High Grain Boundary Recombination Velocity in Polycrystalline Metal Halide Perovskites

Zhenyi Ni[1,†], Shuang Xu[1,†], Haoyang Jiao[1,†], Hangyu Gu[1] Chengbin Fei[1] and Jinsong Huang[1,2 *]

[1]Department of Applied Physical Sciences, University of North Carolina, Chapel Hill, NC 27599, United States

[2] Department of Chemistry, University of North Carolina, Chapel Hill, NC 27599, United States

Understanding carrier recombination processes in metal halide perovskites are fundamentally important to further improving the efficiency of perovskite solar cells, yet the accurate recombination velocity at grain boundaries (GBs) has never been determined, despite of the speculative theory of benign GBs in perovskites. Here we report the determination of carrier recombination velocities at grain boundaries (S_{GB}) of polycrystalline perovskites by mapping the transient photoluminescence pattern change induced by the non-radiative recombination of carriers at GBs. Charge recombination at GBs is revealed to be even stronger than at film surfaces of unpassivated films, with average S_{GB} reaching 2200 – 3300 cm/s. Regular surface treatments do not passivate GBs, because they do not physically reach the GBs, making GBs more detrimental to carrier recombination than grain surfaces. We find a surface treatment using tributyl(methyl)phosphonium dimethyl phosphate which can penetrate into GBs by partially dissolving perovskite GBs and converting it into one-dimensional perovskites. It reduces the average S_{GB} by four times, with the lowest S_{GB} of 410 cm/s which is comparable to the surface recombination velocity after passivation.

Introduction

Understanding carrier recombination behaviors in metal halide perovskite materials and devices are important for improving the performance of perovskite optoelectronic devices.[1] Metal halide perovskites have achieved great progresses in photovoltaic application with rapid increase of the power conversion efficiency of perovskite solar cells from 3.8% to 25.5%,[2-4] and in other applications of radiation detectors,[5,6] light detectors[7,8] and light-emitting diodes[9] with performance comparable or better than existing technologies. While the bulk and surface recombination in perovskites have been widely studied, carrier recombination at the hidden grain boundaries (GBs) of polycrystalline perovskite films that are adopted in most of the state-of-the-art high-performance devices have not been well understood, leaving behind the ongoing debate whether GBs are benign or detrimental to device performances.[10]

Different studies have come to inconsistent conclusions on the role of GBs in determining the performance of perovskite solar cells. GBs were speculated to be benign without introducing mid-gap deep trap states,[11-13] while they were also deemed to be non-radiative recombination centers thus being detrimental to solar cells,[10,14,15] or they were involved in a more complicated relationship with the solar cell performance which was also related to the grain size and thickness of perovskite films[16-21]. Conclusions of these studies, however, were mostly drawn empirically by investigating the relationship between solar cell performance and grain sizes, which could mistakenly confuse the effect of grain-size-changing induced crystalline quality and point defects on device performance and not give precise descriptions about the carrier recombination at GBs. To date, there is still no direct or microscopic experimental method to quantitatively characterize

the GB charge carrier recombination velocity (S_{GB}) in polycrystalline perovskites.

On the other hand, passivations of perovskite polycrystalline thin films on multi-levels are shown globally to be indispensable to achieve high performance solar cells.[22,23] While the effect of surface/interface passivation for perovskite thin films has been well demonstrated, the often-speculated GB passivation by different kinds of passivators has not been rigorously verified due to the lack of a direct characterization technique. This raises an undetermined question whether surface treatments of polycrystalline perovskites can also passivate defects at GBs.

In this work, we showed a method which can directly determine S_{GB} in polycrystalline perovskites. The influence of GB recombination on carrier diffusion in perovskite grains is visualized by the transient photoluminescence mapping pattern evolution induced by the charge recombination at GBs. A model is established to quantitatively describe the relationship between S_{GB} and carrier diffusion profiles. We evaluated the GB passivation effect for perovskite thin films with different surface treatment approaches, providing important guidelines for the further improvement of perovskite solar cell performance with desired passivation strategies.

Results and discussion

Fig. 1a and Supplementary Figure 1a show the schematic diagram of using confocal transient photoluminescence mapping (TPLM) and carrier diffusion imaging system to determine S_{GB}. The S_{GB} is derived by measuring the carrier diffusion within a perovskite grain with the confocal system, where the evolution of PL intensity (I_{PL}), which is represented by carrier density n, can be descripted by a two-dimensional (2D) partial differential equation:[24,25]

$$\frac{\partial n}{\partial t} = D\nabla^2 n - An - Bn^2 - Cn^3 \quad (1)$$

where $n = n(x, y, t)$ is the spatial distribution of carrier density at time t, A, B, C are monomolecular, bimolecular, and Auger charge recombination rates, respectively, and D is the diffusion coefficient (Supplementary Figure 1 and Note 1). Surface recombination may reduce the total recombination lifetime but does not affect the 2D carrier diffusion behaviors. Two different boundary conditions are considered depending on the distance (L_{GB}) of the laser excitation spot to the GB. When L_{GB} is larger than the diffusion length of carriers L_D, almost all the PL signal is collected before the photo-excited carriers reach GBs, and an isotropic carrier diffusion behavior is guaranteed. The boundary condition will be

$$\vec{n} \cdot \nabla n(x, y, t) = 0, \quad (2)$$

where $\vec{n}$ is the outward unit normal vector. Otherwise, the boundary condition involving S_{GB} of

$$\vec{n} \cdot \nabla n(x, y, t) + \frac{S_{GB}}{D} n(x, y, t) = 0|_{(x,y)} \quad (3)$$

is applied. In this case GB recombination should cause anisotropic carrier diffusions along the normal direction of the GB, leading to asymmetric PL profile distributions (Fig. 1a).

To illustrate how S_{GB} affects carrier diffusion behaviors, we simulated the dynamic process of carrier diffusion near the GBs with small and large S_{GB} based on equations (1) and (3) (detailed in Supplementary Note1). The initial carrier concentration distribution was implemented with a 2D Gaussian function, simulating the light distribution of a laser spot (Supplementary Figure 1b). Supplementary Videos 1 and 2 show the dynamic diffusion process for S_{GB} = 1 and 10^4 cm/s, respectively, normalized to the peak value for each frame. Fig. 1b shows selected frames from the videos. The light spots expand asymmetrically along different in-plane directions accompanied by

a shifting of emission peak positions, indicating anisotropic carrier diffusions near the GB due to the influence of charge recombination at GBs. Figs. 1c-d plot the detailed PL intensity profiles at different time delays after laser excitation along the *x* direction as labeled in the figure for S_{GB} = 1 and 10^4 cm/s. When S_{GB} is small (1 cm/s), the PL intensity profile asymmetrically broadens toward the GB with its peak shifting toward the GB (Fig. 1c). This can be explained by the reduced carrier density at the GB side due to the moderate charge recombination, generating a descending carrier density gradient toward the GB which drives the diffusion of excess carriers to the GB. A small S_{GB} implies a weak carrier recombination and long-living carriers, enabling a carrier density accumulation at the GB (Fig. 1c and Supplementary Figure 2a). In contrast, when S_{GB} is sufficiently large (10^4 cm/s), the carrier density at the GB is almost zero at any time (Fig. 1d and Supplementary Figure 2b). In this case, the peak of the PL intensity profile shifts away from the GB, due to the fast quenching of charge carriers at GBs that drags down the carrier concentration closing to GBs (Fig. 1d). This simulation result shows that the charge recombination at GBs can cause the PL intensity pattern change, which provides a quantifiable method to determine S_{GB} by fitting the measured PL intensity profiles near the GB (Fig. 1e).

To verify it experimentally, we first determine the parameters *D*, *A*, *B* and *C* by placing the light excitation spot at the center of a grain, and then move the light excitation spot close to the GBs (L_{GB} < 1 μm) to measure PL intensity profile variation over time using transient PL mapping measurement. In this measurement, the spatial distribution of photoluminescence at the sample surface is projected onto an image plane through a telescopic relay lens system, and scanned by an optical fiber mounted on a precise *x*-*y* piezo motor stage which guides light into a single photon

photodetector (See experimental details). By measuring the carrier density propagation from the grain center, we derived D from the relationship $\sigma^2(t) = 2Dt + \sigma_0^2$, where $\sigma^2(t)$ is the mean-square-distribution of the Gaussian-distribution-fitted PL profile along one propagation direction at the time delay t after the laser excitation, and σ_0^2 is the initial mean-square-distribution at $t = 0$.[26-28] By fitting the measured confocal TRPL and PL profiles with equation (1) and boundary condition (2), we obtain recombination rate constants A, B and C. The S_{GB} is then calculated by fitting the measured carrier diffusion profiles along the normal direction of the GB with simulations based on equation (1) and boundary condition (3).

We first used the surfaces of single crystal to represent GBs and measured the surface recombination velocities (S_{Surf}) of freshly cleaved methylammonium lead iodide ($MAPbI_3$) and methylammonium lead bromide ($MAPbBr_3$) single crystals (as illustrated in Fig. 2a), because there are other reported methods to measure S_{Surf} which can be used to verify this method. We also compared S_{Surf} of $MAPbBr_3$ single crystals with and without ozone-treatment ($MAPbBr_3$-O_3) which was reported obviously to modify the S_{Surf}.[29] As shown in Supplementary Figures 3-5, the diffusivities for $MAPbI_3$ and $MAPbBr_3$ crystals measured by the diffusion method are 0.67 and 0.49 cm^2/s, respectively, which are close to previously reported values measured by TPLM or time-of-flight (ToF) methods (Supplementary Table 4).[30,31] By fitting the TRPL and PL profile results, we obtained the values of A, B and C for $MAPbI_3$ and $MAPbBr_3$ single crystals, as summarized in Supplementary Figure 6 and Table 1. Next, we moved the laser excitation spots to near the crystal edge with $L_{GB} = \sim 0.6$ μm, and performed the same carried diffusion measurement. Figs. 2b-c show the measured carrier diffusion profile and PL profiles along the normal direction of the crystal edge

for the $MAPbI_3$ single crystal, respectively. Supplementary Video 3 shows the dynamic PL spreading process by carrier diffusion. For the $MAPbI_3$ single crystal, the peak gradually shifted to the crystal edge after laser excitation, indicating an accumulation of carriers at the crystal edge and thus a small S_{Surf}. For $MAPbBr_3$ single crystals with fresh surface, the peak of the PL profile only slightly merged to the crystal edge after laser excitation, and then moved away from the surface (Figs. 2e-f). The measured trace of the peak shifting along the normal direction of crystal surface can be well fitted with the simulated curve with S_{GB} = 102 ± 45 cm/s for $MAPbI_3$ crystals, and 400 ± 190 cm/s for $MAPbBr_3$ crystals with fresh surfaces (Figs. 2d and g), showing the bromide crystals have much stronger surface charge recombination. Statistic results of S_{GB} and simulations with different D and L_{GB} are shown in Supplementary Figures 7-10. After ozone treatment, the average S_{Surf} of $MAPbBr_3$ is reduced to 150 ± 40 cm/s (Figs. 2h-j and Supplementary Figures 11), which is consistent with the previous discovery that O_3 could effectively passivate $MAPbBr_3$ single crystal surface.[29] We then measured S_{Surf} of the $MAPbI_3$, $MAPbBr_3$ and $MAPbBr_3$-O_3 single crystals with the reported surface TRPL measurement that conducted directly on the surface of the crystals (Supplementary Note 2 and Figure 12). The S_{Surf} is derived from surface recombination lifetime τ_S [32,33]:

$$\frac{1}{\tau_S} = \frac{2\alpha^2 D}{1+\sqrt{1+8\alpha^2 D^2/{S_{\mathrm{Surf}}}^2}}, \quad (4)$$

where α is the absorption coefficient at the excitation wavelength. The derived S_{Surf} are 60, 650 and 210 cm/s for $MAPbI_3$, $MAPbBr_3$ and $MAPbBr_3$-O_3 single crystals, respectively, which are close to those obtained from our diffusion method. This validates the effectiveness of our method

in determining the S_{GB} by charge recombination induced transient PL pattern change.

We then investigated the S_{GB} of polycrystalline perovskite thin films. We chose $MAPbI_3$ and $Cs_{0.08}FA_{0.92}PbI_3$ (FA is formamidinium) thin films for this study which are two very typical compositions which showed high solar cell device performance.[34] We mainly chose grains with lateral sizes > 3 μm so that the carrier diffusion near the studied GBs was not affected by adjacent GBs within the time range of measurement (*e.g.*, 20 ns). The interplay of multiple GBs could make a difference to the carrier diffusion behavior,[24] while it is not within the scope of the current study. Fig. 3a shows the PL mapping image of a pristine $MAPbI_3$ thin film. We first measured the D of individual grains by focusing the laser spot onto the grain center (inset of Fig. 3a). Figs. 3b-c show the measured and simulated carrier density profiles and PL profiles for a pristine $MAPbI_3$ grain, respectively. To rule out the possible influence from the unrecombined background carrier density accumulated in the space-limited grains on the Gaussian fitting of the PL profiles, we checked the accuracy of the PL profile fitting obtained with different laser repetition rates, as shown in Supplementary Figure 13. An up-to 20 MHz laser repetition rate was chosen to ensure a negligible influence from the background carrier density on the calculation of D while retaining a high carrier population rate to minimize the measurement duration. In addition, we checked the light stability of the perovskite films, of which the PL intensity change was less than ± 5% within the measurement time of 20 – 30 mins (Supplementary Figure 14).

The average D derived from statistic measurements on multiple pristine $MAPbI_3$ and $Cs_{0.08}FA_{0.92}PbI_3$ grains are ~ 1.0 and 1.1 cm^2/s, respectively (Supplementary Figures 15a-b, 16a-b 19a and Tables 2 and 3). Next, we performed different surface treatments to the $MAPbI_3$ and

$Cs_{0.08}FA_{0.92}PbI_3$ thin films, including $(C8\text{-}NH_3)_2SO_4$ (sulfate) and tributyl(methyl)phosphonium dimethyl phosphate (TPDMP). Passivating perovskite surface by forming a lead sulfate layer with sulfate treatment[35,36] or forming phosphonium lead halide compounds using phosphonium salts[37,38] have been previously demonstrated to reduce surface defects for perovskites. The phosphate-base anion in TPDMP is chosen to further passivate under-coordinated lead ions by forming ionic bonding. After sulfate and TPDMP treatments, both the $MAPbI_3$ and $Cs_{0.08}FA_{0.92}PbI_3$ thin films exhibited significantly enhanced surface PL intensities (Supplementary Figures 20a-b). However, it is unknow whether these passivation agents can reach and passivate GBs as well. To uncover this puzzle, we then characterize the S_{GB} of $MAPbI_3$ and $Cs_{0.08}FA_{0.92}PbI_3$ thin films before and after sulfate and TPDMP treatments.

First, it is noticed that these surface treatments do not affect the D for $MAPbI_3$ and $Cs_{0.08}FA_{0.92}PbI_3$ thin films (Supplementary Figures 15c-f, 16c-f, 19a, Tables 2 and 3), which is reasonable because surface treatments should not change the bulk properties of the perovskite grains. By fitting the recombination rate constants A, B and C from the confocal TRPL and PL profile results (Supplementary Figures 17 and 18), it is seen that bimolecular charge recombination rate remained unchanged before and after surface treatments of both $MAPbI_3$ and $Cs_{0.08}FA_{0.92}PbI_3$, because this is an intrinsic material property for perovskites. In contrast, the trapping related charge recombination is smaller for surface-treated films, indicating that these surface treatments did passivate the surface of the perovskite thin films (Supplementary Figures 19b-c, Tables 2 and 3).

Then we measured the carrier diffusions near GBs for both $MAPbI_3$ and $Cs_{0.08}FA_{0.92}PbI_3$ thin films before and after surface treatments. Typical carrier diffusion profiles along the normal

directions of the GBs and their corresponding PL mapping images are shown in Fig. 3d. Statistic results of the carrier diffusion profiles for multiple grains are shown in Supplementary Figures 21-26. We can see that for pristine and sulfate-treated $MAPbI_3$ and $Cs_{0.08}FA_{0.92}PbI_3$ thin films, the peaks of the diffusion profiles monotonously shift to the center of the grain after laser excitation, indicating a strong GB recombination in these films. While for TPDMP treated films, the peak first shifted toward the GBs and then moved to the grain center. By fitting the traces of the peak shifting for these films with simulation results, we obtain the S_{GB} for each film, as shown in Fig. 3e and f. For pristine $MAPbI_3$ thin films, the S_{GB} varies between 2000 to 5000 cm/s for different grains with an average S_{GB} of 3300 ± 1040 cm/s. The large deviation of the S_{GB} values for different grains indicates a large grain-to-grain heterogeneity in polycrystalline perovskite thin films in terms of grain boundary recombinations.[39] Sulfate treatment does not significantly reduce the GB recombination, as it renders a similar average S_{GB} of 3100 ± 950 cm/s. In contrast, TPDMP surface treatment reduces the S_{GB} to 1200 ± 640 cm/s, with a lowest S_{GB} of about 410 cm/s for about 25% grains measured. Similar results were obtained for $Cs_{0.08}FA_{0.92}PbI_3$ thin films. The pristine and sulfated-treated films have a S_{GB} of 2200 ± 460 cm/s, while TPDMP-treated films show much smaller S_{GB} of 900 ± 490 cm/s. These results demonstrate that TPDMP surface treatment can also passivate GBs for polycrystalline perovskite thin films, which is very different from sulfate treatment.

To understand why TPDMP can passivate the GBs of perovskite polycrystalline films, we first performed PL and atomic force microscopy-infrared (AFM-IR) measurements to check whether these passivation agents could really reach the GBs. As shown in Supplementary Figures

20c-d, the PL intensity from the bottom side was basically unchanged in sulfate treated films, while significantly enhanced in TPDMP treated films, indicating that TPDMP did infiltrate into the perovskite films after surface treatment. For the AFM-IR measurement, we chose IR signals at wavenumbers of 965 cm^{-1} which corresponds to C-H bending vibrations in tributyl(methyl)phosphonium (TP) ions and 1713 cm^{-1} which corresponds to C=N stretching in FA to distinguish the IR response from the passivation agents/reaction production and $Cs_{0.08}FA_{0.92}PbI_3$ perovskite (Supplementary Figure 27).[40] We did not use $MAPbI_3$ for the IR measurement due to the overlapping of C-H vibration IR signals between MA and TP ions. As shown in Figs. 4a-b, for TPDMP treated $Cs_{0.08}FA_{0.92}PbI_3$ films, both the GBs and grain surfaces show high IR signals at wavenumber of 965 cm^{-1}, while the GBs have much lower IR signals at 1713 cm^{-1} wavenumber compared to the grain surfaces. In contrast, the pristine films show negligible IR signals around GBs at all the wavenumbers (Fig. 4a). This indicates that TP ions not only cover grain surface but also penetrate into GBs of polycrystalline perovskite films and accumulate there. Then we further revealed the GB passivation mechanism by investigating the chemical reactions between TPDMP and perovskites. As shown in Supplementary Note 3 and Figure 28, TPDMP can readily react with perovskite and dissolve it at room temperature. The top surface PL intensities of perovskite films decreased after coating of TPDMP without annealing, and then significantly enhanced after annealing. XRD results show that the reaction between TPDMP and perovskite at room temperature generates an intermediate phase first, which eventually turned into $TPPbI_3$ after annealing (Supplementary Figure 28). The PL intensity change at the bottom interface followed the same trend with top surface, suggesting the TPDMP penetrated through the whole perovskite

films. This is further supported by unchanged PL intensity for the sulfate surface treatment which only change the top surface (Supplementary Figure 20). These results reveal that the penetration of TP ions into perovskites along GBs occurred by the quick conversion of 3D perovskite surface and grain boundaries into a liquid intermediate phase first, and then the intermediate phase is converted to a one-dimensional (1D) perovskite via the reaction during annealing at 100 °C:[41]

$$TP^{+} + [PbI_3]^{-} \rightarrow TPPbI_3 \quad (5)$$

which can passivate the GBs, as schematically illustrated in Fig. 4c.

To compare the GB and surface passivation capabilities of TPDMP, we directly measured the S_{Surf} of $Cs_{0.08}FA_{0.92}PbI_3$ films before and after surface treatment by the same carrier diffusion measurements. To do it, we need to rotate the sample and measure the cross-sections of these films with geometry shown in Fig. 4d. Fig. 4e shows the PL mapping images for the cross-sections of pristine, sulfate- and TPDMP-treated $Cs_{0.08}FA_{0.92}PbI_3$ thin films deposited on glass. We focused the laser spot near the top surface of the grains for each film and performed the carrier diffusion measurement. Fig. 4f and Supplementary Figure 30 show the traces of peak shifting along the normal direction of the grain surface for these films. Statistical S_{Surf} values are summarized in Fig. 3f. It is noteworthy that the S_{Surf} was slightly smaller than the S_{GB} for pristine $Cs_{0.08}FA_{0.92}PbI_3$ films (1800 *vs.* 2200 cm/s), indicating that GBs are even more detrimental to carrier recombination than the surface for $Cs_{0.08}FA_{0.92}PbI_3$ films. After sulfate treatment, the S_{Surf} is reduced to 1000 ± 490 cm/s, validating the surface passivation effect by sulfate treatment. For the TPDMP treated films, the average S_{Surf} is similar to S_{GB}, as both are around 900 cm/s. This highlights that TPDMP has good passivation effects for both the grain surfaces and GBs.

After knowing S_{Surf} and S_{GB} for perovskite single crystals and polycrystalline thin films, we further estimated the surface and GB interfacial trap densities (N_t) by using $S = N_t \sigma v_{th}$ (where σ is the capture cross-section for electrons or holes which is estimated to be 10^{-15} cm^2 and v_{th} is the thermal velocity which is 10^7 cm/s).[42-44] As shown in Fig. 4g, the surface trap densities of $MAPbI_3$ and $MAPbBr_3$ single crystals are around 10^{10} cm^{-2}, while that of polycrystalline thin films are over 10^{11} cm^{-2}. For pristine polycrystalline thin films, the trap densities at GBs of about 3×10^{11} cm^{-2} are slightly higher than that at grain surfaces.

To make this method easy to use, we develop a fast quantification method to derive S_{GB} for perovskites by using one simplified parameter d_{max}/L_{GB}, where d_{max} is the maximum displacement of the carrier profile peak-shifting toward the GB, as schematically illustrated in Fig. 5a. The dependence of the normalized peak shifting d_{max}/L_{GB} on S_{GB} for our perovskites with D varying from 0.1 to 2 cm^2/s is plotted in Fig. 5b. This provides a quick estimation of S_{GB} (applies for S_{Surf} as well) for most perovskites by simply measuring the relative displacement of the carrier profile peak-shifting with respect to the total distance to GBs. To verify the applicability of this quantification method for perovskites, we checked the influences of L_{GB}, recombination rate coefficients A and B on the quantitative relationship between d_{max}/L_{GB} and S_{GB}, as shown in Supplementary Figures 31 and 32. It is seen that the variations of L_{GB}, A and B from 0.4 to 0.8 μm, 0.2 to 1 ns^{-1} and 10^{-4} to 2×10^{-3} cm^2/s, respectively, which safely cover the ranges of all the measured values for perovskites in this work, have negligible influence on the dependence of d_{max}/L_{GB} on S_{GB}, thus validating the universal application of Fig. 5b for most perovskites.

In summary, we establish a characterization method which is able to determine the GB

recombination velocity at microscopic scales in polycrystalline perovskite thin films, and evaluate the passivation effect at the hidden GBs by different passivation agents. We demonstrate that regular surface passivation methods like sulfate treatment can only passivate grain surface while not GBs, making GB detrimental to solar cell performance. A new surface passivation method using TPDMP can passivate both grain surface and boundaries, pointing out a promising future direction for the further improvement of perovskite solar cells by passivating GBs via simple surface treatments.

Reference

1 Huang, J., Yuan, Y., Shao, Y. & Yan, Y. Understanding the physical properties of hybrid perovskites for photovoltaic applications. *Nat. Rev. Mater.* **2**, 17042 (2017).

2 https://www.nrel.gov/pv/cell-efficiency.html

3 Min, H. *et al.* Perovskite solar cells with atomically coherent interlayers on SnO_2 electrodes. *Nature* **598**, 444-450 (2021).

4 Chen, S. *et al.* Stabilizing perovskite-substrate interfaces for high-performance perovskite modules. *Science* **373**, 902-907 (2021).

5 Zhao, J. *et al.* Perovskite-filled membranes for flexible and large-area direct-conversion X-ray detector arrays. *Nat. Photonics* **14**, 612-617 (2020).

6 Zhou, Y. *et al.* Heterojunction structures for reduced noise in large-area and sensitive perovskite x-ray detectors. *Sci. Adv.* **7**, eabg6716 (2021).

7 Kim, W. *et al.* Perovskite multifunctional logic gates via bipolar photoresponse of single photodetector. *Nat. Commun.* **13**, 720 (2022).

8 Fang, Y., Dong, Q., Shao, Y., Yuan, Y. & Huang, J. Highly narrowband perovskite single-crystal photodetectors enabled by surface-charge recombination. *Nat. Photonics* **9**, 679 (2015).

9 Ma, D. *et al.* Distribution control enables efficient reduced-dimensional perovskite LEDs. *Nature* **599**, 594-598 (2021).

10 An, Q. *et al.* Small grains as recombination hot spots in perovskite solar cells. *Matter* **4**, 1683-1701 (2021).

11 Yin, W. J., Shi, T. & Yan, Y. Unique properties of halide perovskites as possible origins of the superior solar cell performance. *Adv. Mater.* **26**, 4653-4658 (2014).

12 Yun, J. S. *et al.* Benefit of Grain Boundaries in Organic-Inorganic Halide Planar Perovskite Solar Cells. *J. Phys. Chem. Lett.* **6**, 875-880 (2015).

13 Yang, M. *et al.* Do grain boundaries dominate non-radiative recombination in $CH_3NH_3PbI_3$

perovskite thin films? *Phys. Chem. Chem. Phys.* **19**, 5043-5050 (2017).

14 Nie, W. *et al.* High-efficiency solution-processed perovskite solar cells with millimeter-scale grains. *Science* **347**, 522-525 (2015).

15 Xu, W. *et al.* Precisely Controlling the Grain Sizes with an Ammonium Hypophosphite Additive for High-Performance Perovskite Solar Cells. *Adv. Funct. Mater.* **28**, 1802320 (2018).

16 Adhyaksa, G. W. P. *et al.* Understanding Detrimental and Beneficial Grain Boundary Effects in Halide Perovskites. *Adv. Mater.* **30**, e1804792 (2018).

17 Jariwala, S. *et al.* Local Crystal Misorientation Influences Non-radiative Recombination in Halide Perovskites. *Joule* **3**, 3048-3060 (2019).

18 Im, J. H., Jang, I. H., Pellet, N., Gratzel, M. & Park, N. G. Growth of $CH_3NH_3PbI_3$ cuboids with controlled size for high-efficiency perovskite solar cells. *Nat. Nanotechnol.* **9**, 927-932 (2014).

19 Kim, H. S. & Park, N. G. Parameters Affecting I-V Hysteresis of $CH_3NH_3PbI_3$ Perovskite Solar Cells: Effects of Perovskite Crystal Size and Mesoporous TiO_2 Layer. *J. Phys. Chem. Lett.* **5**, 2927-2934 (2014).

20 Correa-Baena, J.-P. *et al.* Identifying and suppressing interfacial recombination to achieve high open-circuit voltage in perovskite solar cells. *Energy Environ. Sci.* **10**, 1207-1212 (2017).

21 Castro-Méndez, A. F., Hidalgo, J. & Correa-Baena, J. P. The Role of Grain Boundaries in Perovskite Solar Cells. *Adv. Energy Mater.* **9**, 1901489 (2019).

22 Wei, N. *et al.* Multi-Level Passivation of $MAPbI_3$ Perovskite for Efficient and Stable Photovoltaics. *Adv. Funct. Mater.*, 2108944 (2021).

23 Chen, B., Rudd, P. N., Yang, S., Yuan, Y. & Huang, J. Imperfections and Their Passivation in Halide Perovskite Solar Cells. *Chem. Soc. Rev.* **48**, 3842-3867 (2019).

24 deQuilettes, D. W. *et al.* Impact of Photon Recycling, Grain Boundaries, and Nonlinear Recombination on Energy Transport in Semiconductors. *ACS Photonics* **9**, 110-122 (2021).

25 Deng, S. *et al.* Long-range exciton transport and slow annihilation in two-dimensional hybrid perovskites. *Nat. Commun.* **11**, 664 (2020).

26 Xiao, X. *et al.* Ultrafast Exciton Transport with a Long Diffusion Length in Layered Perovskites with Organic Cation Functionalization. *Adv. Mater.* **32**, 2004080 (2020).

27 Wang, T. *et al.* Protecting hot carriers by tuning hybrid perovskite structures with alkali cations. *Sci. Adv.* **6**, eabb1336 (2020).

28 Stavrakas, C. *et al.* Visualizing Buried Local Carrier Diffusion in Halide Perovskite Crystals via Two-Photon Microscopy. *ACS Energy Lett.* **5**, 117-123 (2020).

29 Wei, H. *et al.* Sensitive X-ray detectors made of methylammonium lead tribromide perovskite single crystals. *Nat. Photonics* **10**, 333 (2016).

30 Saidaminov, M. I. *et al.* Multi-cation perovskites prevent carrier reflection from grain surfaces. *Nat. Mater.* **19**, 412-418 (2020).

31 Musiienko, A. *et al.* Defects in Hybrid Perovskites: The Secret of Efficient Charge Transport. *Adv. Funct. Mater.* **31**, 2104467 (2021).

32 Wang, H., Wong, K. S., Foreman, B. A., Yang, Z. Y. & Wong, G. K. L. One- and two-photon-excited time-resolved photoluminescence investigations of bulk and surface recombination dynamics in ZnSe. *J. Appl. Phys.* **83**, 4773-4776 (1998).

33 Reese, M. O. *et al.* Intrinsic surface passivation of CdTe. *J. Appl. Phys.* **118**, 155305 (2015).

34 Deng, Y. *et al.* Defect Compensation in Formamidinium-Cesium Perovskites for Highly Efficient and Stable Solar Modules. *Nat. Energy* **6**, 633–641 (2021).

35 Yang, S. *et al.* Stabilizing Halide Perovskite Surfaces for Solar Cell Operation with Wide-bandgap Lead Oxysalts. *Science* **365**, 473-478 (2019).

36 Li, X. *et al.* Constructing heterojunctions by surface sulfidation for efficient inverted perovskite solar cells. *Science* **375**, 434-437 (2022).

37 He, Q. *et al.* Surface passivation of perovskite thin films by phosphonium halides for efficient and stable solar cells. *J. Mater. Chem. A* **8**, 2039-2046 (2020).

38 Niu, T. *et al.* Ionic Liquids-Enabled Efficient and Stable Perovskite Photovoltaics: Progress

and Challenges. *ACS Energy Lett.* **6**, 1453-1479 (2021).

39 Tennyson, E. M., Doherty, T. A. S. & Stranks, S. D. Heterogeneity at multiple length scales in halide perovskite semiconductors. *Nat. Rev. Mat.* **4**, 573-587 (2019).

40 George, S. Infrared and Raman characteristic group frequencies: tables and charts. *Wiley, Chichester* (2001).

41 Jiao, H., Ni, Z., Shi, Z., Fei, C. & Huang, J. Perovskite Grain Wrapping by Converting Interfaces and Grain Boundaries into Robust and Water-Insoluble Low Dimensional Perovskites. *Submitted* (2022).

42 McIntosh, K. R. & Black, L. E. On effective surface recombination parameters. *J. Appl. Phys.* **116**, 014503 (2014).

43 Mazhari, B. & Morkoç, H. Surface recombination in GaAs PN junction diode. *J. Appl. Phys.* **73**, 7509-7514 (1993).

44 Ni, Z. *et al.* Resolving Spatial and Energetic Distributions of Trap States in Metal Halide Perovskite Solar Cells. *Science* **367**, 1352-1358 (2020).

Data availability

All data generated or analysed during this study are included in the article and its Supplementary Information.

Acknowledgements

This work was supported by the Center for Hybrid Organic Inorganic Semiconductors for Energy (CHOISE), an Energy Frontier Research Center funded by the Office of Basic Energy Sciences, Office of Science within the US Department of Energy.

Author contributions

Z. N. and J. H. conceived the idea and designed the experiments. Z. N. synthesized perovskite

single crystals, and carried out carrier diffusion measurements. Z. N., H. J., H. G. and C. F. fabricated perovskite thin films and carried out surface treatments. S. X. and Z. N. performed simulations. Z. N. and J. H. wrote the paper, and all authors reviewed the paper. †Z. N., S. X. and H. J. contribute equally to this work.

Competing interests: The authors declare no competing financial interests.

Additional information

Supplementary Information is available for this paper at

Reprints and permissions information is available at http://www.nature.com/ reprints.

Correspondence and requests for materials should be addressed to J. H. (jhuang@unc.edu).

Publisher's note: Springer Nature remains neutral with regard to jurisdictional claims in published maps and institutional affiliations.

Methods

Materials: Unless stated otherwise, all the materials and solvent were purchased from Sigma-Aldrich. Lead iodide (PbI_2) with the purity of 99.995% was purchased from BeanTown Chemical. MAI and MABr were purchased from GreatCell Solar.

Synthesis of perovskite single crystals: The $MAPbI_3$ and $MAPbBr_3$ single crystals were synthesized by inverse temperature crystallization method. The precursor solution for the synthesis of $MAPbI_3$ single crystals were prepared by dissolving MAI and PbI_2 with the molar ratio of 1:1 in γ-butyrolactone (GBL) at a concentration of 1.5 M. The solution was heated at 65 °C with magnetic stirring until the solutes fully dissolved, followed by filtering using PTFE filter with 0.2-μm pore size and injected into a vial. The vial was then placed on a hot plate at the temperature of 75 °C. The temperature was gradually increased to boost the growth of the single crystal. The $MAPbBr_3$ single crystals were synthesized in the same procedure with that for the $MAPbI_3$ single crystals. 1.2 M $MAPbBr_3$ precursor solution was prepared by dissolving MABr and $PbBr_2$ with the molar ratio of 1:1 in dimethylformamide (DMF) solvent and then added into a vial on the hot plate for the crystallization of the single crystals. For the ozone treatment of the $MAPbBr_3$ single crystal, the crystal was firstly cleaved to expose fresh surfaces and then treated with ultraviolet (UV) ozone for 20 mins.

Fabrication of polycrystalline perovskite thin films: For the fabrication of $MAPbI_3$ polycrystalline thin films, glass substrates were first prepared by cleaning with detergent, deionized water, acetone and isopropanol (IPA) in sequence and ultraviolet ozone treatment (20 min). 1.4M $MAPbI_3$ precursor solution was prepared by dissolving MAI and PbI_2 with the molar

ratio of 1:1 in dimethylformamide (DMF) and dimethyl sulfoxide (DMSO) (with the volume ratio of 9:1). 1.5% volume ratio of methylammonium hypophosphite (MAH_2PO_2) was then added to the precursor solution to tune the grain size of $MAPbI_3$ thin films. The precursor solution was spin-coated onto the glass substrate at 2000 rpm for 2s and then 4000 rpm for 20s. During the spin-coating, 130 μl toluene was added into the film at the 8th second. The as-formed film was then heated at 100 °C for 10 min and 120 °C for 10 min. The $Cs_{0.08}FA_{0.92}PbI_3$ perovskite films were fabricated by blade coating method at room temperature under nitrogen knife blowing by using a precursor solution containing 1.0 M $FAPbI_3$ and 0.09 M $CsPbI_3$ dissolved in a 2-methoxyethanol:DMSO solvent mixture. 1.5% volume ratio of MAH_2PO_2 was added to the precursor solution to tune the grain size of $Cs_{0.08}FA_{0.92}PbI_3$. The as-coated solid film was annealed at 150 °C in air for 2 mins. The oxysalt treatment of the polycrystalline perovskite thin films was carried out by spin-coating 2 mM $(C8\text{-}NH_3)_2SO_4$ solution in toluene/isopropyl alcohol mixture on the as-fabricated thin films at 5000 r.p.m for 30s, followed by thermal annealing at 100 °C for 10 min. For the TPDMP treatment, TPDMP solution was prepared by dissolving TPDMP in a TL:IBA = 1:4 solution with a concentration of 4 mM, and followed by dynamic spin-coating onto the perovskite thin films at 5000 rpm for 30s. After the spin-coating, the film was annealed at 100 ℃ for 5 mins. For the fabrication of polycrystalline thin film solar cells, a PTAA solution with the concentration of 2 mg/ml in toluene was spin-coated onto the ITO glass substrate at 4000 r.p.m for 30s, followed by the fabrication of perovskite thin films. The whole device was completed by sequentially thermal evaporating C_{60} (30 nm), BCP (6 nm) and Cu electrodes (80 nm) on the perovskite film.

PL mapping and carrier diffusion measurements: transient photoluminescence mapping and carrier diffusion imaging were measured by PicoQuant Micro Time 100 confocal microscopic system. An Olympus 100× oil immersion objective with a numerical aperture (NA) of 1.45 was used for the measurement. Samples were covered by immersion oil (Olympus Immersion Oil Type-F) in a dark environment during the measurement. Picosecond 640 and 480 nm pulsed lasers with a repetition rate of 20 MHz were used to measure $MAPbI_3$ and $MAPbBr_3$ perovskites, respectively. The focused lasers generated near-Gaussian distributions of light intensities, with full width at half maximum (FWHM) of about 510 and 440 nm for the 640 and 480 nm laser sources, respectively. The average laser intensity was kept at around 36 nW at 20 MHz, corresponding to a photon energy of 1.8 fJ per pulse and an approximate photon flux of 6000 photons per pulse. The PL generated by samples was collected through the same objective, and relayed onto an image plane through a telescopic relay lens system. The transmitted epifluorescence image was then collected by a single photon detector (QicoQuant PMA Hybrid) through an optical fiber which was connected to a precise *x*-*y* piezo motor stage (PI U-751.24) with a linear step resolution of 100 nm. The minimum temporal resolution of the system was 25 ps which was determined by the time-correlated single photon counting modules (TimeHarp 260). Statistical results were collected from more than two batches of samples with over 15 grains for each type of perovskite thin film. The one-photon surface TRPL and PL spectrum measurements were conducted with PicoQuant Fluo Time 300 fluorescence lifetime and steady state spectrometer. A 405 nm pulsed laser with spot size diameter of around 1 mm was used to measure the surface recombination lifetime.

Other characterizations： AFM-IR measurement was carried out by using Bruker nanoIR3 with

tapping mode. The IR laser range was from 900 cm^{-1} to 1900 cm^{-1}. The measurement was calibrated by a Polymethyl methacrylate (PMMA) sample for accurate topography, phase and IR images. XRD spectra were obtained by a Rigaku sixth-generation MiniFlex X-ray diffractometer.

Simulations: all the simulations were performed using Partial Differential Equation (PDE) Toolbox that was implanted in MATLAB, as detailed in Supplementary Information.

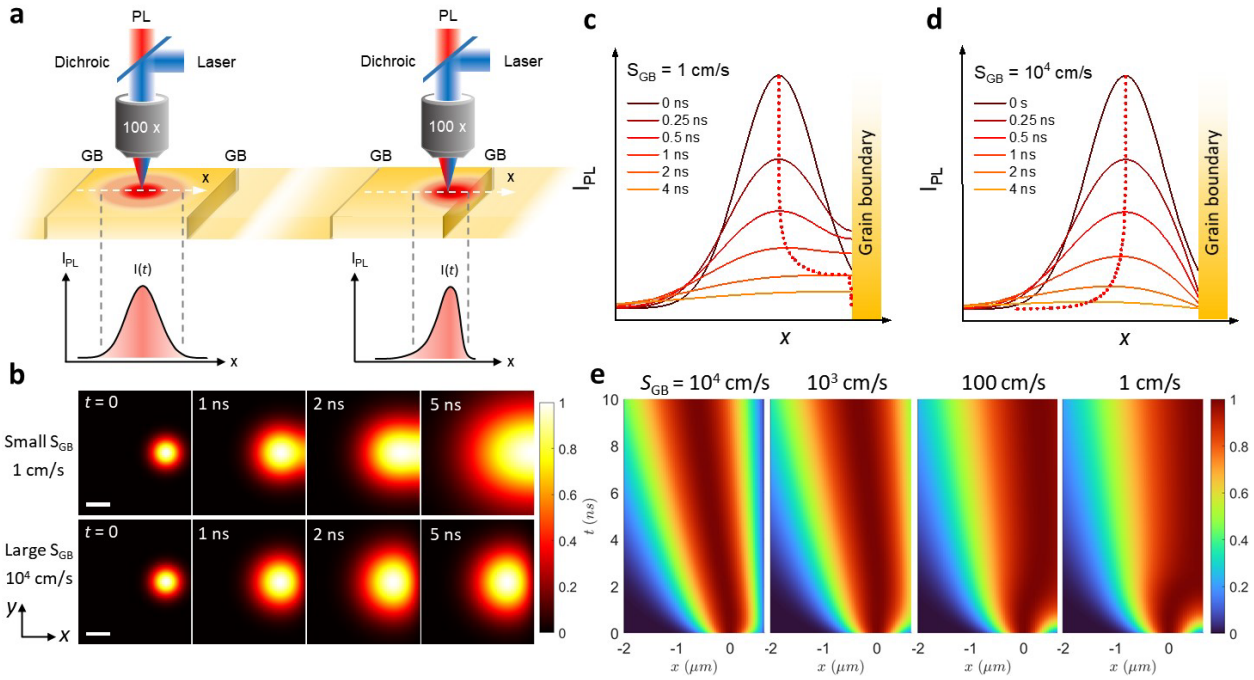

Fig. 1 | Determination of GB charge recombination velocities. a, schematic diagram of using PL mapping and carrier diffusion imaging to measure GB recombination velocities. Excitation laser is focused onto the grain center (left) or near the GB (right) of perovskite films via a 100× oil immersion objective. The carrier diffusion from the laser excitation spot is represented by the red ellipses. The linear PL intensity (I_{PL}) profiles along one direction (x) which is indicated by white dashed lines of the carrier diffusion image plane at time t are representatively shown on the bottom. The grey dashed lines denote the edges of the PL profile curves. **b**, simulated 2D (x-y) carrier diffusion images of perovskite crystals with small (top) and large (bottom) S_{GB} at time frames of 0, 1, 2 and 5 ns. The I_{PL} is normalized to its peak value at each frame. **c**, **d**, simulated linear PL profiles along one direction (x) of the perovskite crystals with S_{GB} = 1 cm/s (**c**) and 10^4 cm/s (**d**) at different times after laser excitation. The red dashed lines denote the shifts of the peak positions of the profile curves. The yellow blocks denote the locations of GBs. **e**, simulated linear carrier diffusion profiles along the normal direction of crystal edges of $MAPbI_3$ single crystals with different S_{GB}. The crystal edge is at the right edge of each figure.

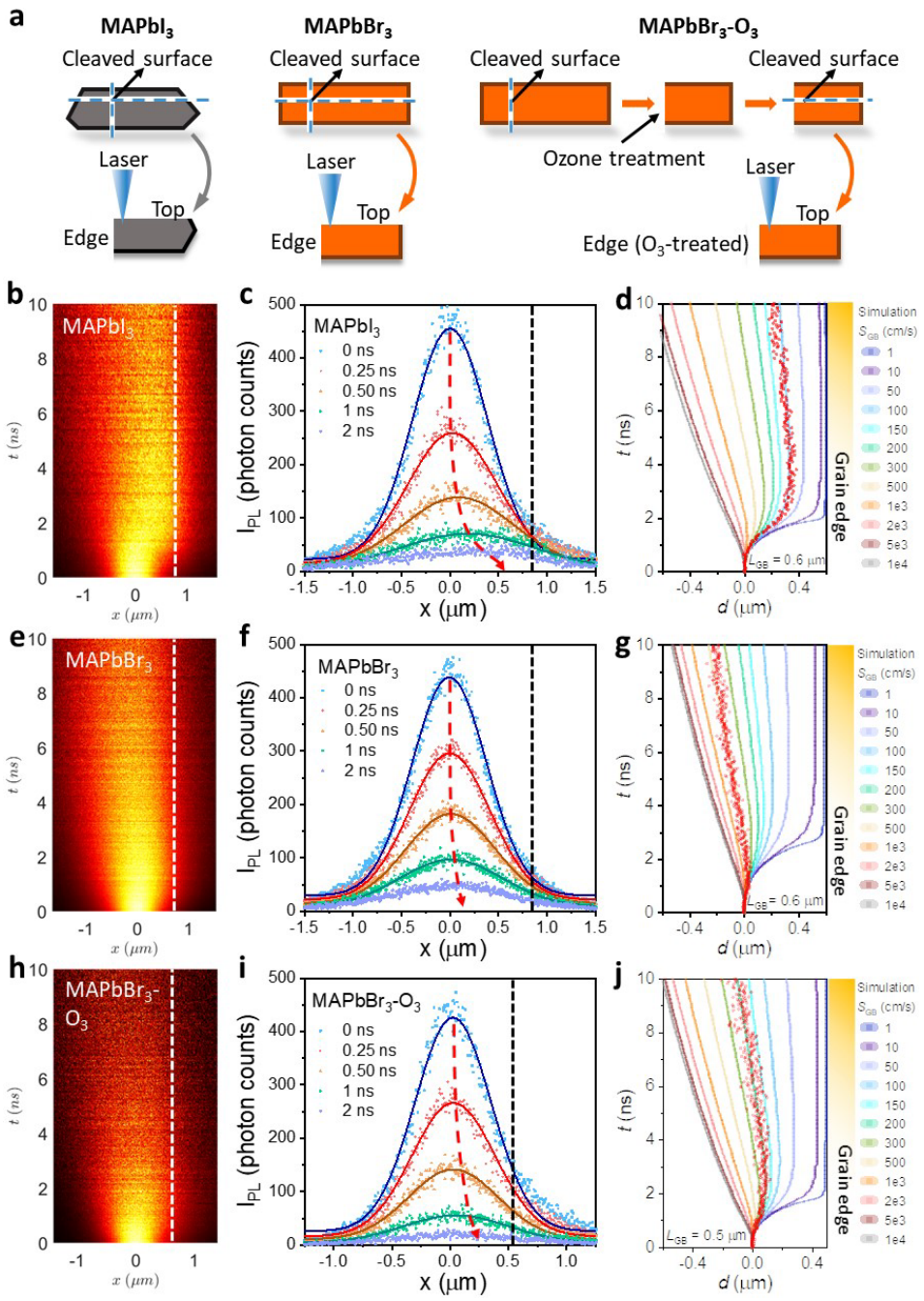

Fig. 2 | Surface charge recombination velocities of perovskite single crystals. a, Schematic illustrations of sample preparation processes for $MAPbI_3$, $MAPbBr_3$ and ozone-passivated $MAPbBr_3$ ($MAPbBr_3$-O_3) single crystals for the measurement of S_{Surf}. Note only the crystal edge of $MAPbBr_3$-O_3 was treated by ozone. **b**, **e**, **h**, measured carrier diffusion profiles near the crystal edges of the $MAPbI_3$ (**b**), $MAPbBr_3$ (**e**) and $MAPbBr_3$-O_3 (**h**) single crystals. The white dashed

lines denote the locations of crystal edges. **c**, **f**, **i**, measured PL intensity profiles near the crystal edges of the $MAPbI_3$ (**c**), $MAPbBr_3$ (**f**) and $MAPbBr_3$-O_3 (**i**) single crystals. The black dashed lines denote the locations of crystal edges. The red dashed lines indicate the peak-shifts of the PL profile curves with time. **d**, **g**, **j**, traces of the peak-shifting with time extracted from (**b**), (**e**) and (**h**) (red dots) overlapped with those obtained from simulation results with different S_{GB} (colored lines) for $MAPbI_3$ (**d**), $MAPbBr_3$ (**g**) and $MAPbBr_3$-O_3 (**j**) single crystals.

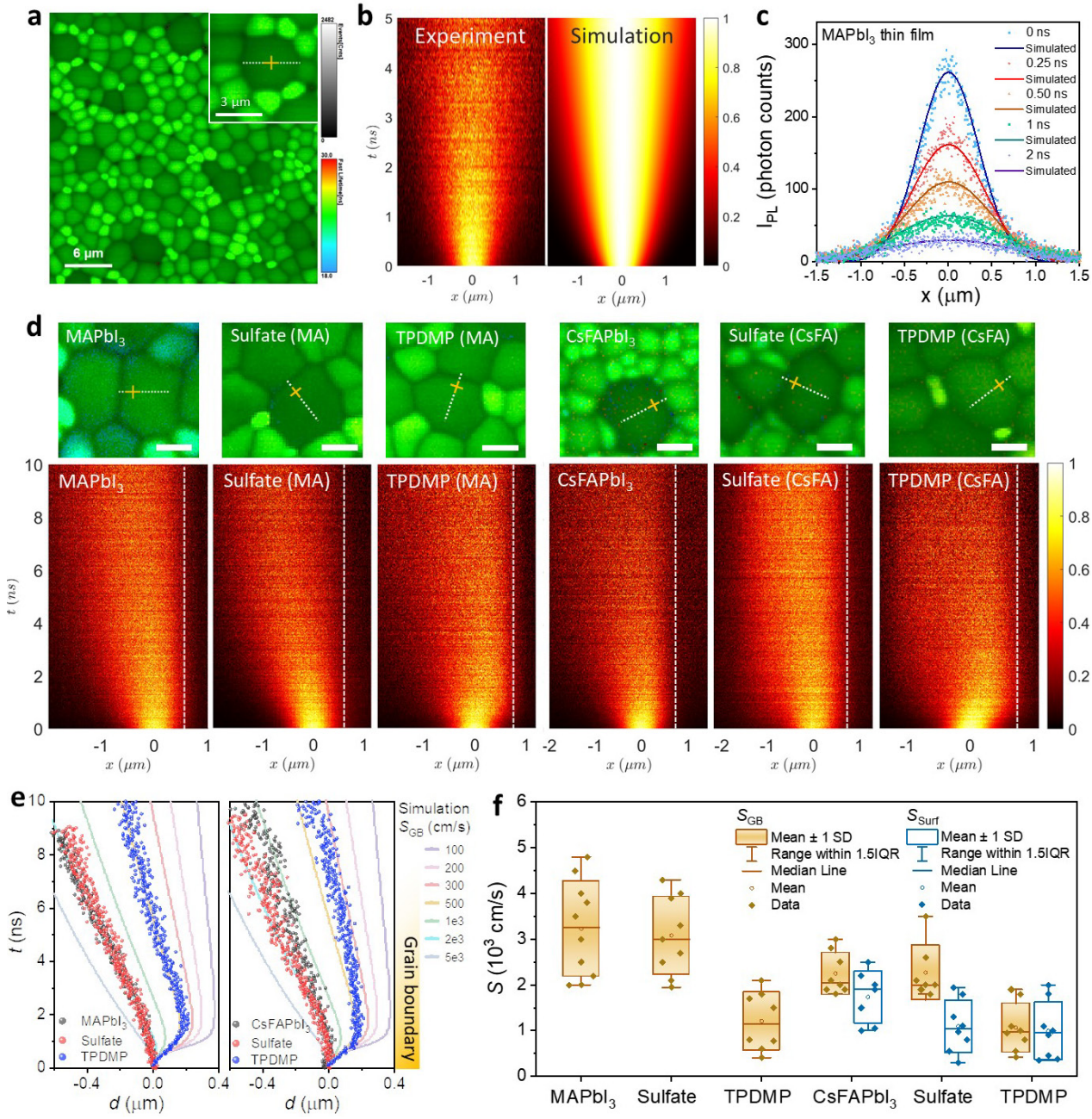

Fig. 3 | GB charge recombination velocities of perovskite thin films with different passivation. **a**, time-resolved PL mapping image of a $MAPbI_3$ polycrystalline thin film. The inset shows the zoomed-in PL mapping image of a $MAPbI_3$ grain. The yellow cross denotes the laser excitation spot, and the white dashed line denotes the direction for the carrier diffusion and PL profiles. **b**, measured (left) and simulated (right) linear carrier diffusion profiles of a $MAPbI_3$ grain in the thin

film when the laser excites the grain center. **c**, measured (dots) and simulated (solid lines) linear PL profiles at different times after excitation of the $MAPbI_3$ grain when the laser excites the grain center. **d**, PL mapping images of pristine, sulfate-, TPDMP-treated $MAPbI_3$ and pristine, sulfate-, TPDMP-treated $Cs_{0.08}FA_{0.92}PbI_3$ grains (top) chosen for carrier-diffusion measurement, and the corresponding carrier diffusion profiles along the normal direction of GBs of these grains (bottom). The yellow crosses in the PL mapping images denote the laser excitation spots which are around 0.6 μm away from the GBs. The white dashed lines denote the directions for the carrier diffusion profiles. Scale bar: 2 μm. The white dashed lines in the diffusion profile images denote the locations of GBs. **e**, overlapping of the measured traces of peak-shifting of carrier diffusion profiles extracted from (**d**) (dots) with those obtained from simulation results for $MAPbI_3$ (lest) and $Cs_{0.08}FA_{0.92}PbI_3$ (right) grains with different S_{GB} (solid lines). The yellow block denotes the location of the GB. **f**, statistic results of S_{GB} of grains in pristine, sulfate- and TPDMP-treated $MAPbI_3$ and $Cs_{0.08}FA_{0.92}PbI_3$ thin films, together with S_{Surf} of pristine, sulfate- and TPDMP-treated $Cs_{0.08}FA_{0.92}PbI_3$ thin films.

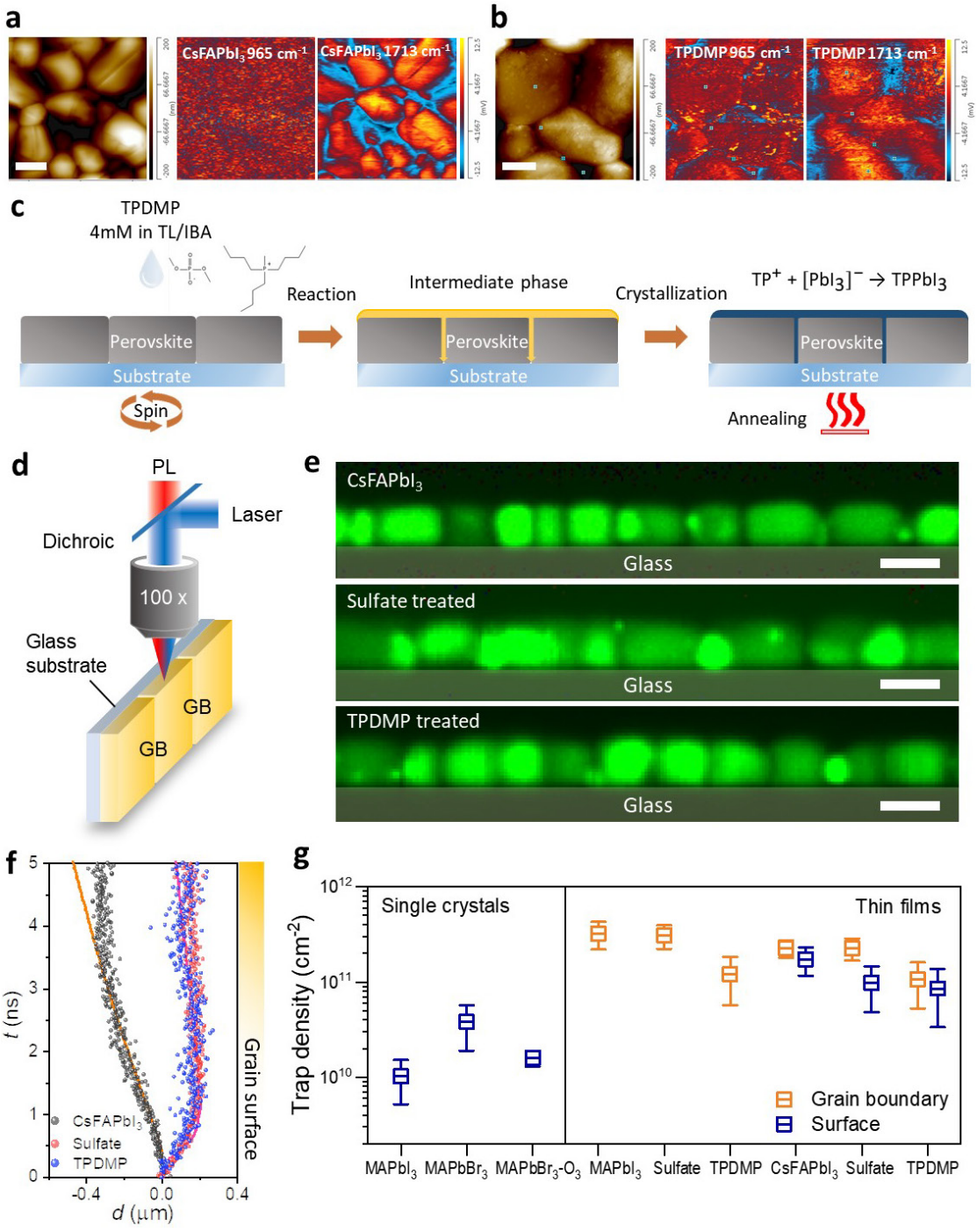

Fig. 4 | Grain boundary passivation of perovskite thin films by TPDMP. a, **b**, AFM topography (left) and IR images of pristine (**a**) and TPDMP-treated (**b**) $Cs_{0.08}FA_{0.92}PbI_3$ polycrystalline thin films measured at wavenumbers of 965 (middle) and 1713 (right) cm^{-1}. Scale bar: 2 μm. **c**, schematic illustration of the grain boundary passivation process by TPDMP. **d**, schematic diagram

of using PL mapping and carrier diffusion imaging to measure the cross-section of polycrystalline perovskite thin films. **e**, time-resolved PL mapping images of cross-sections of pristine, sulfate- and TPDMP-surface-treated $Cs_{0.08}FA_{0.92}PbI_3$ thin films. Scale bar: 2 μm. **f**, overlapping of the measured traces of peak-shifting of carrier diffusion profiles with laser excitations near the grain surfaces of pristine, sulfate- and TPDMP-treated $Cs_{0.08}FA_{0.92}PbI_3$ thin films with simulations results for S_{GB} = 2000 cm/s (orange line) and 300 cm/s (pink line). The yellow block denotes the location of the grain surface. **g**, estimated surface and GB trap densities of perovskite single crystals and polycrystalline thin films.

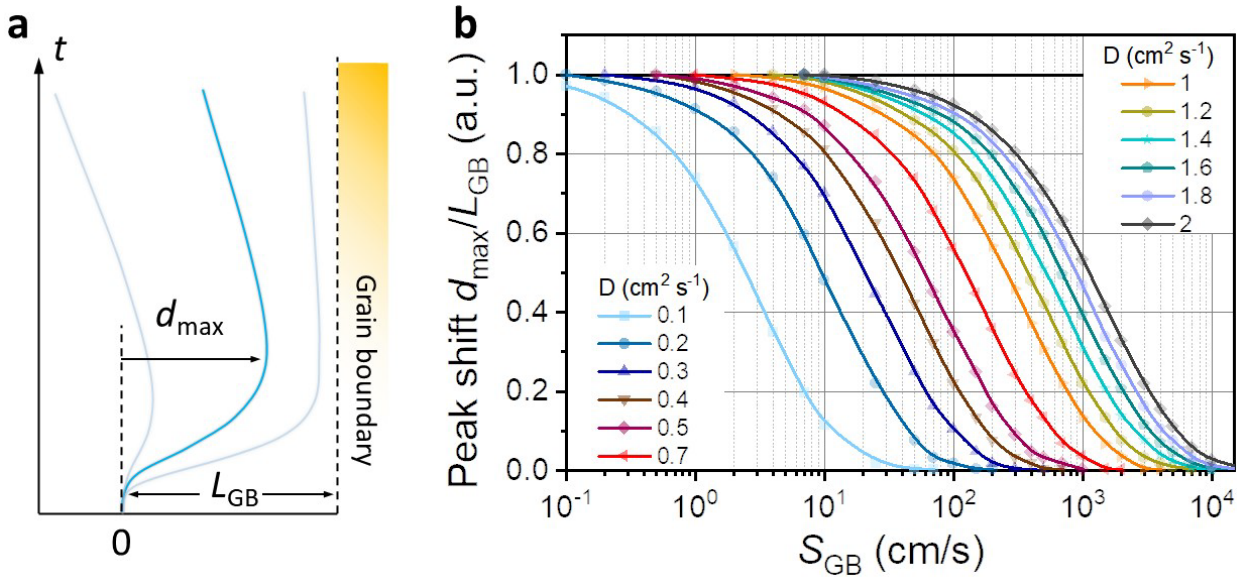

Fig. 5 | Fast quantification of GB charge recombination velocities in perovskites. a, schematics of the variation of the trace of carrier diffusion profile peak-shifting with S_{GB}. The location 0 indicates the laser excitation spot. The bright and dim blue lines plot the traces of the peak-shifting with different S_{GB}. d_{max} is the maximum displacement of the carrier profile peak-shifting toward the GB. **b**, dependence of normalized peak shifting d_{max}/L_{GB} on S_{GB} for perovskites with D varying from 0.1 to 2 cm^2/s. This quantitative relationship is valid for L_{GB}, A and B ranging from 0.4 to 0.8 μm, 0.2 to 1 ns^{-1} and 10^{-4} to 2×10^{-3} cm^2/s, respectively.